

Transformative Nanomedicine of an Amphiphilic Camptothecin Prodrug for Long Circulation and High Tumor Uptake in Cancer Therapy

Fuwu Zhang,[†] Guizhi Zhu,^{*,†} Orit Jacobson,[†] Yi Liu,^{†,‡} Kai Chen,[§] Guocan Yu,[†] Qianqian Ni,[†] Jing Fan,[†] Zhen Yang,[†] Frederick Xu,[†] Xiao Fu,[†] Zhe Wang,[†] Ying Ma,[†] Gang Niu,[†] Xiaobin Zhao,^{||} and Xiaoyuan Chen^{*,†}

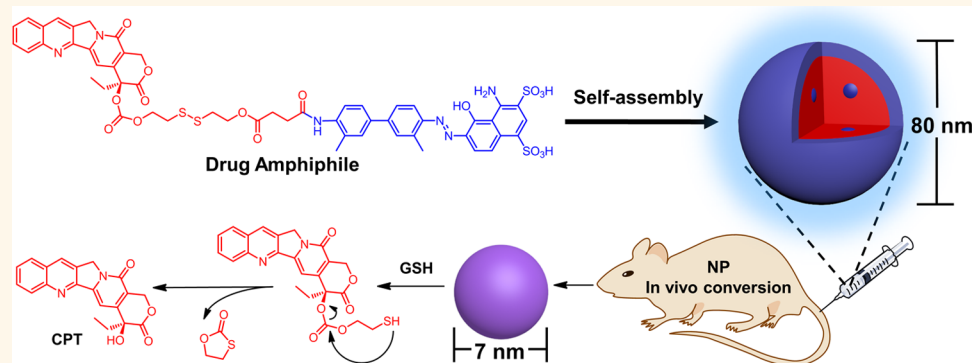
[†]Laboratory of Molecular Imaging and Nanomedicine (LOMIN), National Institute of Biomedical Imaging and Bioengineering (NIBIB), National Institutes of Health (NIH), Bethesda, Maryland 20892, United States

[‡]School of Engineering, China Pharmaceutical University, Nanjing 210009, P. R. China

[§]Molecular Imaging Center, Department of Radiology, Keck School of Medicine, University of Southern California, Los Angeles, California 90033, United States

^{||}The White Oak Group, Washington, D.C. 20006, United States

S Supporting Information



ABSTRACT: We report a camptothecin (CPT) prodrug that was well formulated in solution and rapidly transformed into long-circulating nanocomplexes *in vivo* for highly efficient drug delivery and effective cancer therapy. Specifically, using a redox-responsive disulfide linker, CPT was conjugated with an albumin-binding Evans blue (EB) derivative; the resulting amphiphilic CPT-ss-EB prodrug self-assembled into nanostructures in aqueous solution, thus conferring high solubility and stability. By binding CPT-ss-EB to endogenous albumin, the 80 nm CPT-ss-EB nanoparticles rapidly transformed into 7 nm albumin/prodrug nanocomplexes. CPT-ss-EB was efficient at intracellular delivery into cancer cells, released intact CPT in a redox-responsive manner, and exhibited cytotoxicity as potent as CPT. In mice, the albumin/CPT-ss-EB nanocomplex exhibited remarkably long blood circulation (130-fold greater than CPT) and efficient tumor accumulation (30-fold of CPT), which consequently contributed to excellent therapeutic efficacy. Overall, this strategy of transformative nanomedicine is promising for efficient drug delivery.

KEYWORDS: albumin, camptothecin prodrug, drug delivery, nanostructures, self-assembly

Colorectal cancer is the third most common type of cancer in the United States.¹ Chemotherapy is one of the most important treatments for colorectal cancer, especially those at late stages (III and IV).² Camptothecin (CPT), a potent DNA topoisomerase I inhibitor,^{3,4} has demonstrated remarkable preclinical antitumor activity, but failed in clinical trials due to the low solubility and adverse side

effects.³ Irinotecan (IR), a CPT analogue, was approved to treat colon cancer in 1998 by the U.S. Food and Drug Administration (FDA). Despite the improved aqueous

Received: May 1, 2017

Accepted: August 31, 2017

Published: August 31, 2017

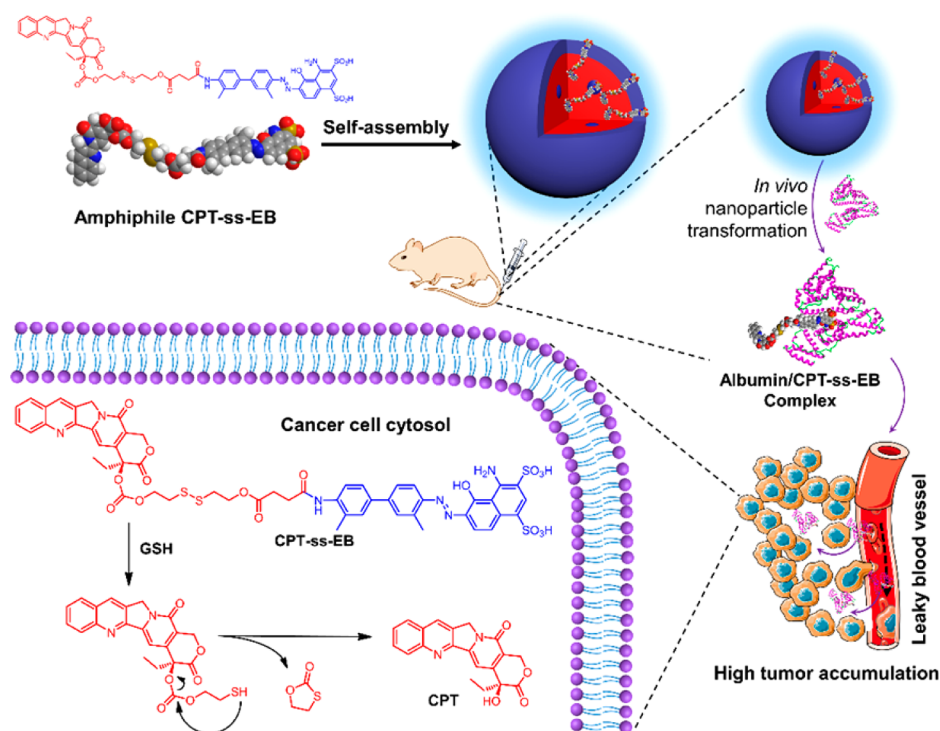
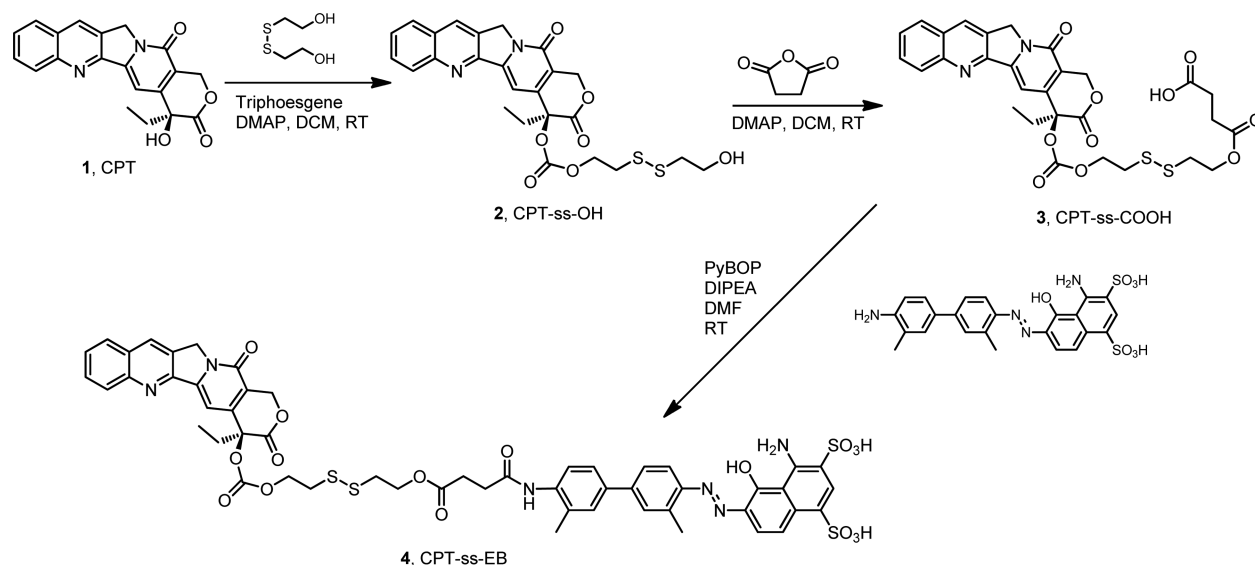


Figure 1. Schematic illustration of transformative nanoparticles of amphiphilic CPT prodrug with prolonged blood circulation, enhanced tumor accumulation, efficient cancer cell uptake, redox-responsive release of intact CPT drug, potent cancer therapeutic efficacy, and low side effects.

Scheme 1. Synthesis of CPT-ss-EB



solubility and reduced side effects, IR has dramatically compromised antitumor potency.^{5,6} Therefore, there are continuous efforts devoted to the effective delivery of CPT, with a focus on nanocarriers.^{5,7–12}

Nanomedicine has been extensively studied for cancer treatment.^{13,14} While plenty of small molecule anticancer agents are hydrophobic, the use of nanoparticles not only improves their aqueous dispersity but also enhances their pharmacokinetics and biodistribution, leading to improved therapeutic efficacy and reduced side effects.^{13,15–19} Toward this end, drug-delivering nanoparticles have been developed from small molecular drug amphiphiles,^{20,21} where a hydro-

phobic drug is connected to a hydrophilic molecule, such as an oligo ethylene glycol (OEG),²² a β -sheet-forming peptide sequence,⁸ or another hydrophilic drug.⁹ Unlike polymer-drug conjugates, small molecule drug amphiphiles can be readily synthesized and are typically monodisperse, with defined chemical structures and high drug loading capacities.^{8,9,22} Further, drug amphiphiles can self-assemble into nanostructures and maintain anticancer activities. However, many of these drug amphiphiles utilized the hydroxyl group on the lactone ring of CPT/IR and formed a rather stable ester linkage, causing extremely slow drug release and significant reduction in cytotoxicity potency.⁷ Moreover, drug amphiphiles

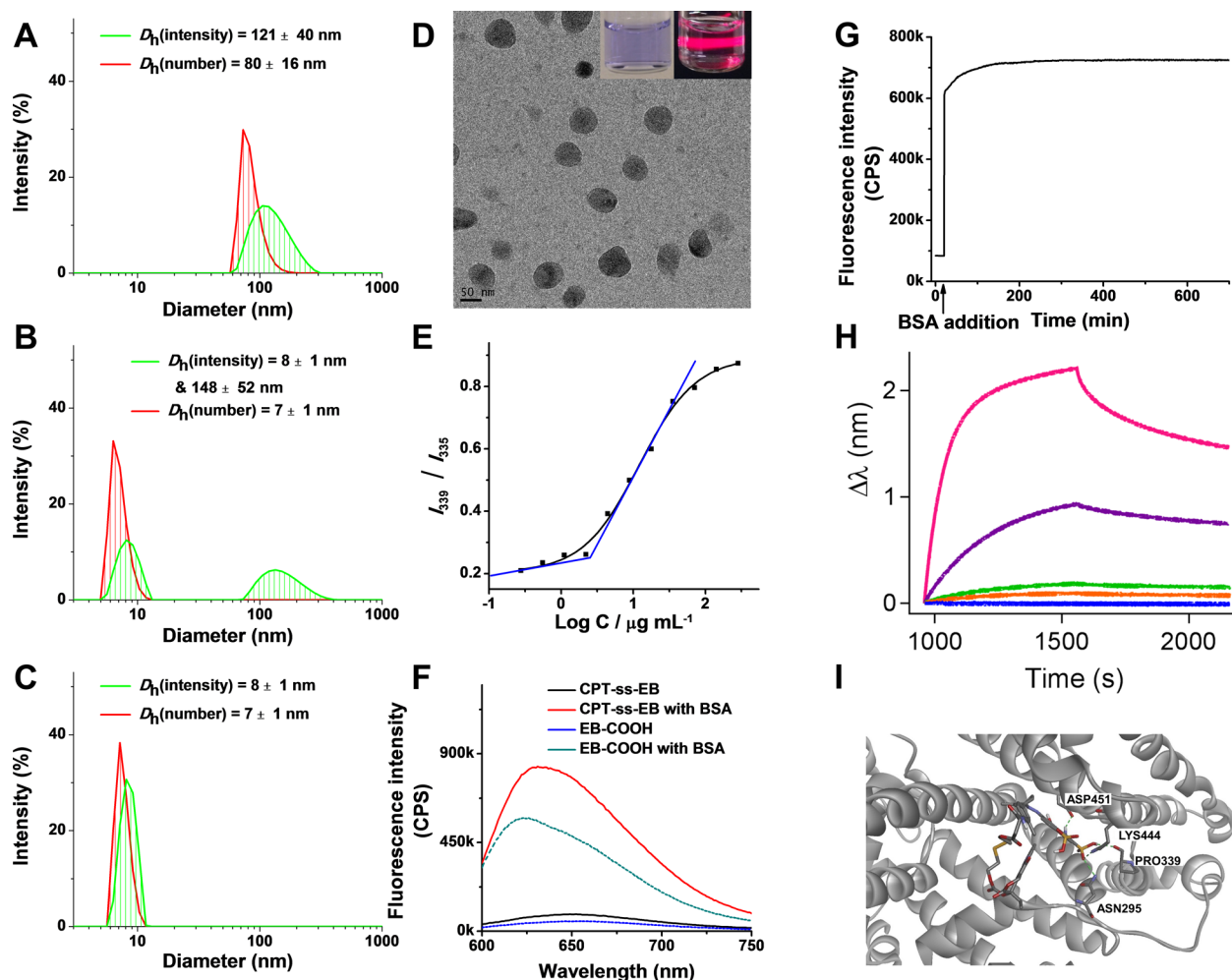


Figure 2. Characterization of transformer nanoparticles of amphiphilic CPT-ss-EB prodrug. (A–C) DLS histograms of CPT-ss-EB nanoparticles in PBS (A), CPT-ss-EB nanoparticles mixed with BSA for 5 min (B) and 24 h (C). (D) A TEM image of CPT-ss-EB nanoparticles; inserts are the photographs of CPT-ss-EB nanoparticles in water in bright field (left) and in the dark with a red laser passing through (right). (E) Plot of the $I_{339\text{ nm}}/I_{335\text{ nm}}$ ratio from pyrene excitation spectra as a function of CPT-ss-EB logarithm concentration. (F) Fluorescence spectra of CPT-ss-EB and EB-COOH in the absence or presence of BSA. (G) Kinetics of albumin binding with CPT-ss-EB as monitored by fluorescence enhancement. (H) Association/dissociation curve of BSA and CPT-ss-EB in PBS at 10, 1, 0.1, 0.01, and 0.001 μM (top to bottom), as measured by BLI. (I) Predicted structure of the CPT-ss-EB/HSA nanocomplex. HSA (gray) is represented in solid ribbon. CPT-ss-EB and the residues in the binding site of HSA are represented in stick. Hydrogen bonds of CPT-ss-EB with interacting amino acid residues in HSA are shown by green dashed lines.

may not maintain their nanostructures *in vivo* where the drug concentration can easily fall below the critical aggregation concentration (CAC) and thus may not benefit from the enhanced permeability and retention (EPR) effect of nanomedicine.^{23,24}

Herein, we report a transformative nanomedicine of amphiphilic CPT prodrug that rapidly transformed from 80 nm stable nanoparticles to 7 nm albumin/prodrug nanocomplexes by avidly binding to endogenous albumin carriers as an approach to formulate hydrophobic drugs and enhance tumor-targeted drug delivery. Specifically, we developed nanomedicines self-assembled from an amphiphilic CPT prodrug, termed as CPT-ss-EB, where CPT was conjugated *via* a redox-responsive disulfide linker with an albumin-binding Evans blue (EB) derivative (Figure 1).^{25–28} Serum albumin is the most abundant protein in the blood, with a blood half-life of ~ 20 days and a size of around 7 nm.²⁹ One of the very first examples of EPR effect was actually conducted using albumin/EB complex in 1986.³⁰ Since then, albumin has been utilized for

delivering various therapeutics,^{31,32} such as the FDA-approved nanoparticle albumin-bound paclitaxel (Abraxane).^{32,33} Therefore, our nanoparticles self-assembled from CPT-ss-EB amphiphiles not only take advantage of chemically defined synthesis and stable formulation of small molecule drugs but also harness endogenous abundant albumin as a drug carrier and benefit from the EPR effect *in vivo* upon transforming to albumin/CPT-ss-EB nanocomplexes. Further, the low concentration of glutathione (GSH) in blood ensures that CPT-ss-EB is stable and remains inactive during circulation, resulting in reduced side effects; whereas the elevated concentration of GSH in cancer cells facilitates drug release upon drug internalization into cells, whereby converting the CPT prodrug into highly toxic CPT.

RESULTS AND DISCUSSION

Synthesis and Characterization of Drug Amphiphiles.

Amphiphilic CPT-ss-EB was synthesized *via* three steps from commercially available CPT and an NH_2 -functionalized EB

derivative (EB-NH₂) (Scheme 1). Briefly, hydroxy-functionalized CPT was activated using triphosgene in the presence of 4-(dimethylamino)pyridine (DMAP) and then reacted with an excess amount of 2,2'-dithiodiethanol to afford prodrug CPT-ss-OH. Succinic anhydride was used to convert the hydroxyl group of CPT-ss-OH into carboxylic acid-terminated CPT-ss-COOH, with DMAP used as a catalyst. The structures of CPT-ss-OH and CPT-ss-COOH were confirmed by ¹H NMR (Figures S1–2). Finally, CPT-ss-COOH was incubated with EB-NH₂ in anhydrous dimethylformamide (DMF), with benzotriazol-1-yl-oxytripyrrolidinophosphonium hexafluorophosphate (PyBOP) as a coupling agent. The product was purified *via* high-performance liquid chromatography (HPLC) and lyophilized into dark blue powder. In the ¹H NMR spectra, the chemical shifts of aromatic protons from both CPT and EB-NH₂ appeared between 7.0 and 9.5 with a nearly 1:1 ratio, demonstrating that CPT-ss-COOH and EB-NH₂ were successfully conjugated (Figure S3). Electrospray ionization mass spectrometry (ESI-MS) and analytical HPLC further verified the synthesis and purity of CPT-ss-EB (Figure S4). CPT-cc-EB, where CPT and EB were conjugated *via* a CH₂CH₂ bridge, was prepared in a similar approach as a control (Figures S5–7). UV–vis also confirmed that both CPT-ss-EB and CPT-cc-EB had the characteristic absorption peaks of CPT (~370 nm) and EB-NH₂ (~316 nm and ~570 nm) in acetonitrile and water mixture (Figure S14). Worth noting, both prodrugs contained as high as >30% CPT.

Lyophilized CPT-ss-EB can be resuspended in aqueous solution and spontaneously self-assemble into nanoparticles as a result of its intrinsic amphiphilic nature. Due to the excellent aqueous solubility of EB and formation of nanoparticles, CPT-ss-EB could be dispersed in water at concentrations as high as 5 mg/mL. When diluted into water, CPT-ss-EB displayed strong light scattering by the Tyndall effect, suggesting the formation of well-defined nanoparticles (Figure 2D inset). Dynamic light scattering (DLS) further revealed that CPT-ss-EB nanoparticles had a hydrodynamic diameter of 80 ± 16 nm and zeta potential of -14 ± 3 mV (Figure 2A and S17). Transmission electron microscopy (TEM) suggested that CPT-ss-EB nanoparticles were spherical with relatively uniform size of *ca.* 57 nm (Figure 2D). Using pyrene as a probe, the CAC of CPT-ss-EB was measured to be as low as 1.5 μg/mL (Figure 2E),⁷ indicating remarkable stability in water. The formation of stable nanoparticles not only enhanced the aqueous dispersity of CPT but also protected it from hydrolysis.³⁴ It was reported that CPT lactone ring hydrolyzed quickly in PBS, with a half-life of 24 min, and only 17% of CPT lactone form remained at equilibrium.³⁴ As monitored by DLS, CPT-ss-EB nanoparticles maintained the hydrodynamic size in PBS over 6 d, further manifesting their colloidal stability (Figure S15). Moreover, after incubating CPT-ss-EB nanoparticles in PBS for 3 d, only a trace amount of degradation products was observed by HPLC, and no free CPT was detected for either drug amphiphiles, further confirming their high stability (Figure S16). Liquid chromatography–mass spectrometry (LC-MS) demonstrated that CPT-ss-EB was quite stable after incubation with BSA or HSA for 24 h. The high stability in aqueous environment, together with excellent capability of repeated lyophilization and resuspension, makes CPT-ss-EB nanoparticles highly attractive as a self-delivery platform.

Although small molecular drug amphiphiles may be stable in aqueous solution, they may not maintain nanostructures *in vivo*. One key feature of CPT-ss-EB amphiphiles is its ability to

convert to an albumin/drug nanocomplex by binding to albumin. The resulting nanoscopic albumin/prodrug nanocomplexes can take advantage of albumin's long blood circulation and EPR effect for preferential accumulation in tumor. A series of studies verified albumin binding ability of CPT-ss-EB. First, a 10-fold increase of the EB fluorescence intensity of CPT-ss-EB in the presence of excess bovine serum albumin (BSA), to an extent comparable to that of unconjugated EB-COOH, verified albumin binding ability of CPT-ss-EB (Figure 2F). In a detailed fluorescence kinetics study (Figure 2G), the EB fluorescence of CPT-ss-EB at 0.2 mg/mL, corresponding to the initial mouse plasma drug concentration after drug injection, was monitored for 20 min, and then albumin was added with a final concentration of 35 mg/mL, corresponding to mouse serum albumin concentration. Immediately after adding albumin, the EB fluorescence increased by 7.3 times and gradually increased by a total of 8.6 times in 4 h. Second, the number-averaged hydrodynamic diameters of CPT-ss-EB nanoparticles changed from 80 to 7 nm right after adding albumin, suggesting that the majority of CPT-ss-EB dissociated from nanoparticles and transformed to albumin/CPT-ss-EB nanocomplexes (Figure 2B). Worth noting, the intensity-averaged hydrodynamic diameters changed from 121 nm for CPT-ss-EB nanoparticles to 148 and 7 nm after adding albumin, indicating the co-presence of albumin/CPT-ss-EB nanocomplexes as well as a small portion of remaining CPT-ss-EB nanoparticles. After 1 day, both number- and intensity-averaged hydrodynamic diameters changed to around 7 nm (Figure 2C). The TEM images also indicated large CPT-ss-EB nanoparticles were transformed into small CPT-ss-EB/albumin nanocomplexes after incubation with BSA (Figure S18). Third, we further studied the binding kinetics of albumin and CPT-ss-EB in PBS using biolayer interferometry (BLI). As shown, classic association/dissociation curves were obtained at different concentrations (Figure 2H). The dissociation constant (K_d) of CPT-ss-EB/albumin was determined to be 1.04 μM ($R^2 = 0.901$), indicating a strong bind affinity of CPT-ss-EB with albumin. Molecular docking of CPT-ss-EB into the human serum albumin (HSA) demonstrated a similar result, with a K_d of 39 μM. The sulfonic acid of CPT-ss-EB shows the interaction with the HSA residues Asn²⁹⁵, Pro³³⁹, Lys⁴⁴⁴, and Asp⁴⁵¹ through hydrogen bonds (Figure 2I). Furthermore, ESI-MS and LC-MS also confirmed that CPT-ss-EB could form nanocomplexes with BSA/HSA (Figures S19–21, one or two CPT-ss-EB molecules per protein). Together, these results demonstrated that CPT-ss-EB nanoassemblies were able to bind to albumin and subsequently transform into CPT-ss-EB/albumin nanocomplexes.

The release of CPT from amphiphilic CPT-ss-EB nanoparticles was evaluated by a dialysis method (Figure 3). CPT-ss-EB was very stable in PBS without GSH and released only ~3% CPT over 72 h. In contrast, >80% of CPT was rapidly released within 12 h in the presence of 10 mM GSH, confirming that the disulfide bond was readily cleaved by GSH, which subsequently led to the breakdown of the carbonate bond to release intact CPT. When the GSH concentration was 1 mM, a slightly slower release of CPT from CPT-ss-EB was observed, with ~61% CPT released at 12 h. At 50 μM GSH concentration, the release of CPT was significantly inhibited, and only ~13% of free CPT was detected. These results suggest that CPT-ss-EB would be relatively stable under normal physiological conditions, such as saline, bloodstream, and extracellular matrix, but rapidly release CPT inside cells,

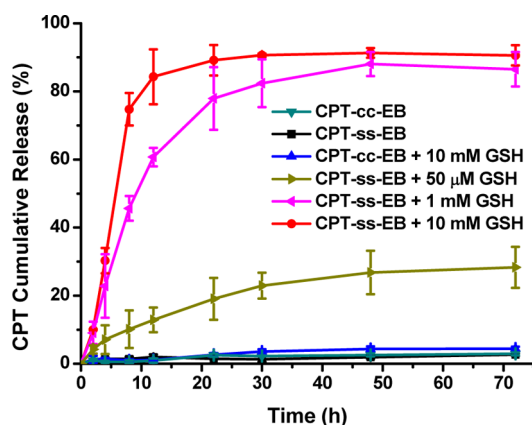


Figure 3. *In vitro* CPT release in PBS with/without GSH over 3 d at 37 °C in PBS, as measured by a dialysis method. The increase of CPT concentration was determined by HPLC. The release was evaluated in triplicate.

especially cancer cells whose GSH level is elevated. Worth noting, the thiol from albumin may also trigger the release of CPT, although at a much slower rate than GSH (Figure S23). As expected, CPT-cc-EB barely released CPT (<5%) in PBS with or without GSH, indicating the high stability of ester linkage under such conditions.

***In Vitro* Cellular Uptake and Cytotoxicity of Drug Amphiphilic Nanoparticles.** We then investigated the cellular uptake of drug amphiphiles by super-resolution confocal microscopy and flow cytometry. Since EB is fluorescent, these drug amphiphiles were directly imaged without additional dye labeling. After 2 h incubation with cancer cells in medium containing albumin, CPT-ss-EB (Figure 4A) was localized mainly in the cytoplasm and part of the nuclei of HCT116 colon cancer cells. Worth noting, CPT could also be imaged due to its blue fluorescence, which had a decent colocalization with EB at 2 h (Figure 4A). When CPT-ss-EB was incubated for a longer period of 4 h, increased blue fluorescence from CPT was detected in the cell nuclei as

compared to the red fluorescence of EB (Figure S25). The altered distribution of CPT and EB indicated the breakage of disulfide bond intracellularly by the endogenous GSH. The released CPT more likely entered the cell nuclei over EB, leading to the different localization of fluorescence. Super-resolution confocal microscopy of single cells clearly revealed that EB fluorescence was localized with endolysosome, suggesting that drug amphiphiles entered cells through an endocytic pathway (Figures 4B and S24). The cellular uptake of different drug formulations was further studied by flow cytometric analysis. Both CPT and EB fluorescence intensities were dramatically enhanced in HCT116 cells treated with either CPT-ss-EB or CPT-cc-EB, in contrast to the low fluorescence intensity of cells treated with free CPT or IR (Figure 4C,D), demonstrating effective uptakes of these amphiphilic prodrug nanoparticles in cancer cells.

Motivated by the high cellular uptake, we studied the *in vitro* cytotoxicities of prodrug nanoparticles in multiple cancer cell lines (Figure 5). In HCT116 colon cancer cells, the IC_{50} value of CPT-ss-EB was 0.15 μM , which was comparable to that of the highly potent CPT (0.087 μM), 12-fold lower than that of FDA-approved IR (1.8 μM), and 286-fold lower than that of CPT-cc-EB (43 μM). This demonstrated the potent cytotoxicity of CPT-ss-EB prodrugs and that the cleavable disulfide linkage in CPT-ss-EB is critical for optimal intracellular drug release and cytotoxicity. As indicated in the release experiment, the ester linkage in the CPT-cc-EB was quite stable in aqueous environment, where only *ca.* 3% of free CPT was released over 3 d. The stable linkage led to significantly reduced cytotoxicity.^{8,9,22} The low toxicity of CPT-cc-EB also implies that CPT-ss-EB may have slow drug liberation and low toxicity during blood circulation where GSH concentration is low. In U87MG cells, CPT-ss-EB also displayed potent cytotoxicity, with an IC_{50} value (0.31 μM) comparable to that of free CPT (0.12 μM). Further, in 4T1 and A549 cancer cells, the cytotoxicity of CPT-ss-EB was also comparable to CPT, though these cells were generally less sensitive to any of these formulations compared with HCT116 cells. Together, these

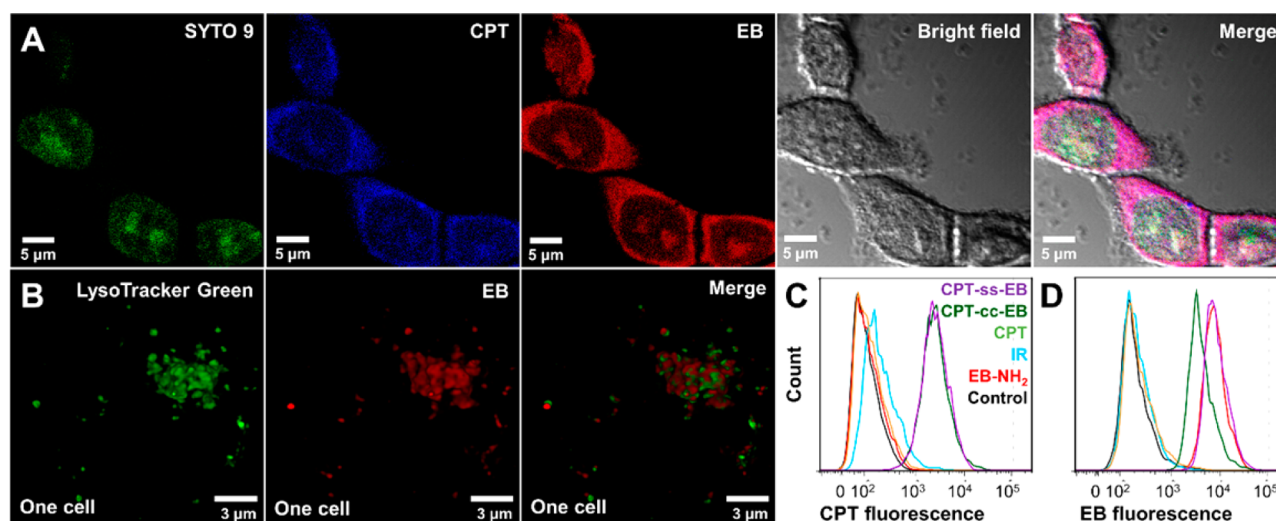


Figure 4. Efficient uptake of transformative prodrug amphiphiles into cancer cells. Confocal microscopy images showing multiple cells (A) and super-resolution confocal microscopy images showing one single cell (B), demonstrating cellular internalization of CPT-ss-EB into the endolysosome of HCT116 cells. Blue: CPT fluorescence; green in A: SYTO 9 (nuclear stain); green in B: LysoTracker Green (lysosomes); and red: EB fluorescence from CPT-ss-EB. (C, D) Flow cytometric analysis of the CPT fluorescence (C) and EB fluorescence (D) of HCT116 cells that were incubated with CPT-ss-EB or controls for 3 h.

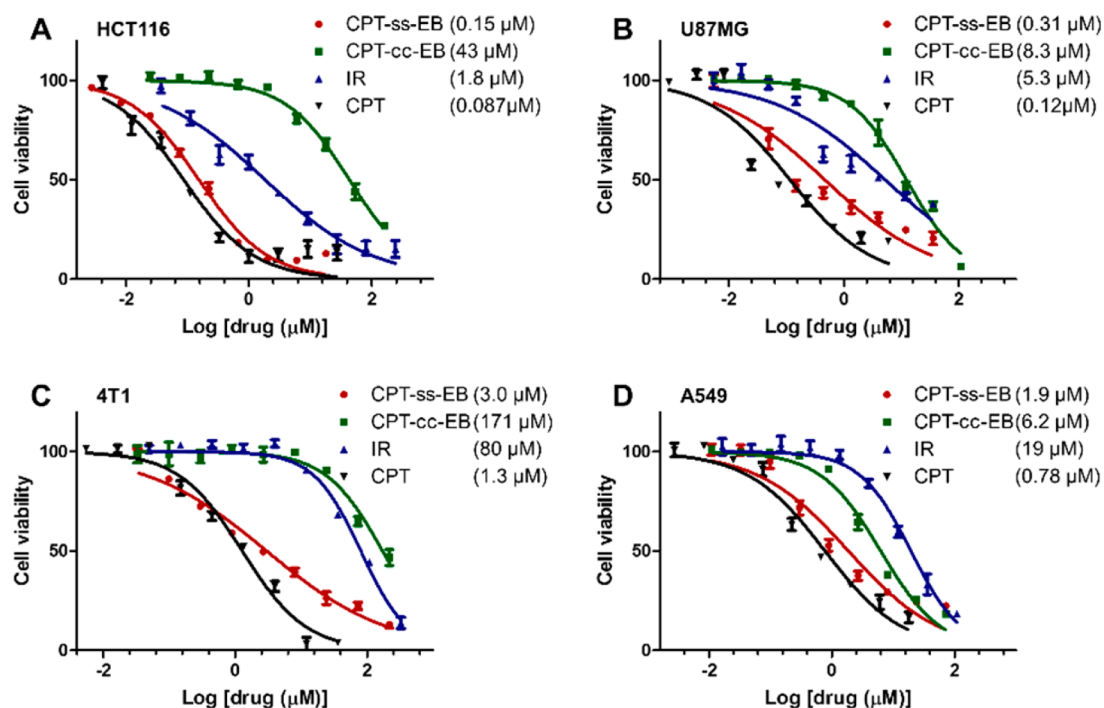


Figure 5. *In vitro* cytotoxicities of CPT-ss-EB, CPT-cc-EB, IR, and CPT against HCT116 (A), 4T1 (B), U87MG (C), and A549 (D) cancer cells. Numbers in parentheses are corresponding IC_{50} values calculated by GraphPad Prism 5.

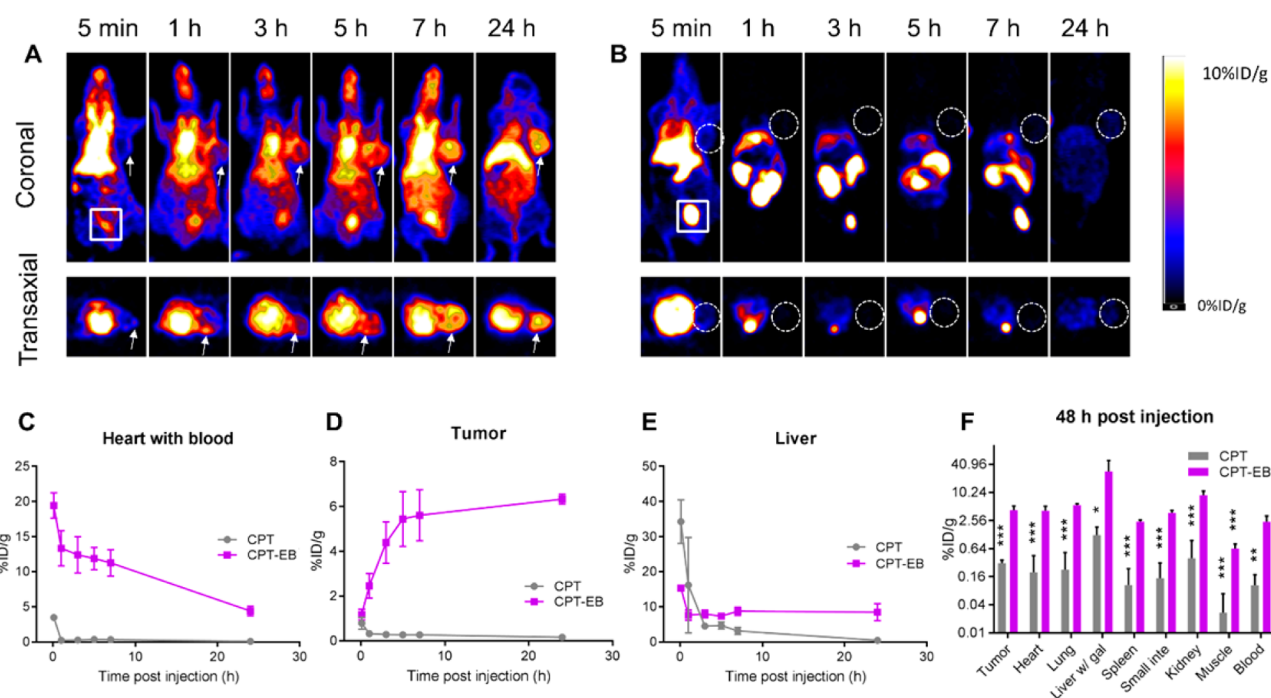


Figure 6. *In vivo* pharmac-imaging. (A, B) Representative whole-body coronal and transaxial PET images of HCT116 tumor-bearing mice at 5 min, 1, 3, 5, 7, and 24 h after intravenous injection of ^{64}Cu -labeled CPT-EB (A) and CPT (B). White arrow/circle indicates the location of tumor. White square indicates bladder. ID/g: injection dose per gram of tissue. The distribution of CPT-EB and CPT in heart (C, with blood), tumor (D), and liver (E) at different time points after injection. The drug concentration was quantified based on decay-corrected PET images ($n = 3/\text{group}$). (F) The biodistribution of drugs determined by γ -counting of excised organs at 48 h post-injection. Data represent mean \pm standard error ($n = 3/\text{group}$). *: $p < 0.05$, **: $p < 0.01$, ***: $p < 0.001$. Statistical significance represents differences between the %ID/g of CPT and CPT-EB in the corresponding organs/blood.

studies demonstrated that CPT-ss-EB prodrug nanoparticles had comparable *in vitro* cytotoxicity with the parent CPT and was much more effective than CPT-cc-EB or the FDA-approved IR.

Prolonged Blood Circulation Half-Life and Enhanced Tumor Uptake of CPT-EB Nanoparticles. The amphiphilic prodrug was next studied for tumor-targeted drug delivery by PET pharmac-imaging in tumor-bearing mice. With the ability

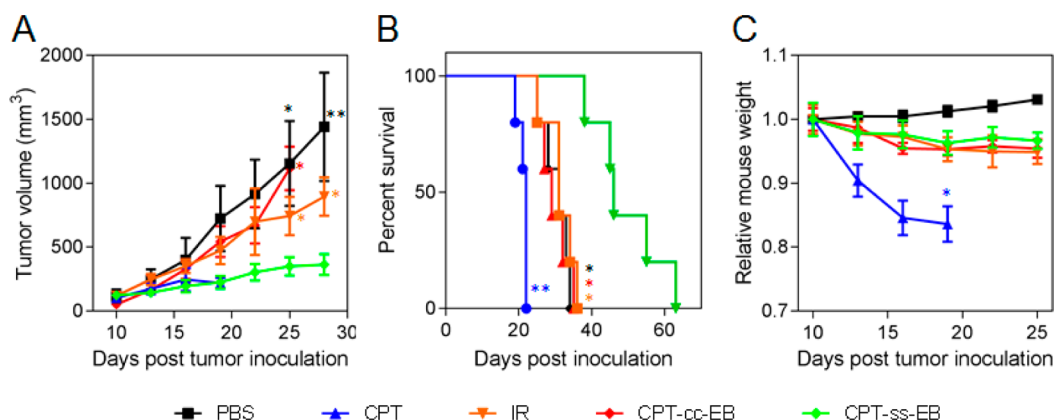


Figure 7. Transformative CPT-ss-EB nanomedicine significantly inhibited tumor progression and dramatically reduced side effects in an HCT116 human colon cancer model. (A) The growth curves of HCT116 tumor after treatment, which was initiated on day 10 post-tumor inoculation, and drugs were intravenously injected every 3 days for 5 times unless mice were euthanized ($n = 5/\text{group}$). CPT-treated mice started to be euthanized at day 18 because of serious morbidity resulting from the toxicity of CPT. (B) Survival rate of HCT116 tumor-bearing mice in each group after intravenous injection of formulations ($n = 5/\text{group}$). (C) Relative body weight of HCT116 tumor-bearing mice in each group after intravenous injection of formulations ($n = 5/\text{group}$). *: $p < 0.05$; **: $p < 0.01$. Asterisks represent statistically significant differences between mice treated with CPT-ss-EB and mice treated with other treatments.

of amphiphilic CPT-EB nanoparticles to transform into a nanoscopic albumin/prodrug nanocomplex by *in vivo* binding with ubiquitous endogenous albumin, we hypothesize that CPT-EB will have prolonged the blood circulation and enhanced tumor accumulation, compared to CPT. To test our hypothesis, we radiolabeled CPT-EB and CPT with ⁶⁴Cu (half-life: 12.6 h) and quantitatively determined their pharmacokinetics and biodistribution. For ⁶⁴Cu radiolabeling through chelation, both CPT-EB and CPT were conjugated with chelator 1,4,7-triazacyclononane-1,4,7-triacetate (NOTA) to afford NOTA-CPT-EB and NOTA-CPT (Schemes S2 and S3; LC-MS results in Figures S8–13). BLI measurement demonstrated that NOTA-CPT-EB had comparable albumin binding affinity to CPT-cc-EB and CPT-ss-EB, with a K_d value of 1.51 μM (Figure S22).

We then intravenously injected ⁶⁴Cu-labeled compounds into HCT116 tumor-bearing mice, followed by PET imaging at 5 min, 1, 3, 5, 7, and 24 h post-injection. CPT-EB gradually accumulated in the tumor, as displayed in the whole-body PET images (Figure 6A, left), while only marginal tumor accumulation of CPT was found (Figure 6B, right). After 24 h, there was a sharp contrast between the accumulation of CPT-EB and CPT in tumor (Video S1). We further quantified the distribution of CPT-EB and CPT in the heart, tumor, and liver at different time points based on decay-corrected PET images. As shown in Figure 6C, the blood concentration of CPT-EB slowly decreased over time, with a half-life of ~ 6.5 h (Figure S17). In contrast, CPT concentration in the blood decreased rapidly, with a half-life of only ~ 3 min (Figure S26). Within 24 h, the area under the curve (AUC) of blood CPT-EB concentration was 221 ± 18 h*%ID/g (ID/g: injection dose per gram of tissue), which was 30-fold larger than that of CPT concentration in blood (7.3 ± 1.2 h*%ID/g). The 130-fold increase of circulation half-life and 30-fold increase of tumor accumulation clearly demonstrated that CPT-EB had a much longer blood retention time over CPT. More importantly, the tumor uptake of CPT-EB increased rapidly from $1.18 \pm 0.24\%$ ID/g at 5 min to $5.61 \pm 1.14\%$ ID/g at 5 h and $6.33 \pm 0.22\%$ ID/g at 24 h (Figure 6D). In contrast, only $0.79 \pm 0.27\%$ ID/g of CPT was accumulated in tumor at 5 min post-injection, and the CPT amount in tumor rapidly vanished (Figure 6D). The

sharp decrease of CPT concentration was probably due to the high liver uptake, where it was digested and excreted from the body (Figure 6E) and rapid renal clearance as suggested by high drug signal in bladder especially at early time points (Figure 6B). *Ex vivo* quantification of organ radioactivity by γ -counting at 48 h post-injection also confirmed the more efficient accumulation of CPT-EB over CPT in the tumor tissues with $4.26 \pm 0.97\%$ ID/g of CPT-EB (Figure 6F). Literature survey showed the average nanoparticle delivery to a tumor was only about 0.7% ID,³⁵ whereas the CPT-EB had a much higher drug delivery efficiency of $>4.0\%$ ID after 48 h. Worth noting, there was a significant amount of radioactivity in the kidneys, indicating CPT-EB may dissociate from the reversibly bound albumin and partially excrete from the body through renal clearance. These studies undoubtedly demonstrated that our CPT-EB prodrug nanoassemblies prolonged drug circulation and preferentially accumulated in tumor, compared to free CPT.

Potent Antitumor Activities and Reduced Side Effects of CPT-ss-EB Nanoparticles. Encouraged by the excellent *in vitro* cytotoxicity and high tumor accumulation *in vivo*, these prodrug nanoparticles were further investigated for tumor therapy in a HCT116 tumor-bearing xenograft model. On day 10 post-subcutaneous inoculation of 5×10^6 HCT116 cells, mice were randomly divided into 5 groups ($n = 5/\text{group}$) and were given the following formulations intravenously every 3 days for maximally 5 times: PBS, CPT, IR, CPT-cc-EB, and CPT-ss-EB. As shown in Figure 7A, CPT-ss-EB displayed the most potent antitumor effects and dramatically delayed tumor progression. In consistency with the poor *in vitro* cytotoxicity, the antitumor activity of CPT-cc-EB was rather limited compared to the redox-sensitive CPT-ss-EB counterpart. The FDA-approved IR showed only moderate antitumor efficacy. Importantly, mice treated with CPT-ss-EB did not show any morbidity during the course of treatment (Figure 7B); however, mice treated with CPT suffered from serious weight loss (by 20%) and lesions at injection sites (Figure 7C) and therefore had to be sacrificed before day 22 post-inoculation (Figure 7B). These results clearly demonstrated that transformative CPT-ss-EB nanoparticles elicited potent therapeutic efficacy and reduced side effects. Motivated by the outstanding

therapeutic efficacy of CPT-ss-EB nanomedicine in the HCT116 tumor, the therapeutic efficacy of CPT-ss-EB nanomedicine was further studied in 4T1 murine breast cancer, which is refractory to many chemotherapeutics such as CPT, as shown by *in vitro* IC₅₀ of 1.3 μ M, compared with 0.087 μ M for HCT116 cells (Figure 5). While neither IR nor CPT-cc-EB significantly inhibited 4T1 tumor growth in BALB/c mice, CPT-ss-EB significantly inhibited 4T1 tumor progression with negligible side effects (Figure S27). These results suggest that CPT-ss-EB may serve as an alternative therapy option for therapeutically refractory tumor.

CONCLUSIONS

In summary, we have designed and synthesized transformative amphiphilic prodrug nanoparticles that were self-assembled *in vitro* from CPT-ss-EB prodrug amphiphiles with a redox-responsive disulfide linker and were transformed to albumin/prodrug nanocomplexes *in vivo* upon avid binding to endogenous albumin. The drug amphiphiles can be facilely synthesized and were intrinsically monodisperse with defined chemical structures and high drug loading content. CPT-ss-EB were directly resuspended into aqueous solution and self-assembled into well-defined nanoparticles with a diameter of 80 \pm 16 nm. The formation of nanoparticles further provided the prodrug amphiphiles with high water dispersity and protected the drug from hydrolytic degradation. Indeed, the drug amphiphiles were stable in PBS with negligible drug degradation for over 6 days. Amphiphilic CPT-ss-EB nanoparticles were efficiently internalized by cancer cells into the endolysosome, leading to potent cytotoxicity in multiple cancer cells with IC₅₀ 1 order of magnitude lower than the FDA-approved IR and comparable to the parent CPT. The cleavable disulfide linker, which would break promptly in the presence of GSH and release intact CPT, was essential to maintain anticancer activities of CPT-ss-EB drug amphiphiles. Compared with polymeric nanoparticles, one potential drawback of most small molecular drug amphiphiles is their relatively low stability in diluted conditions during *in vivo* blood circulation. In our design, *via* binding with endogenous albumin, administered CPT-EB in blood would instantaneously transform from 80 nm nanoparticles into 7 nm albumin/prodrug nanocomplexes. PET pharmaco-imaging in tumor-bearing mice revealed that, compared to parent CPT, our transformable prodrug amphiphiles prolonged blood circulation by 130-fold and enhanced tumor accumulation of drugs by 30-fold in 1 day. These remarkable pharmacokinetics and tumor uptake capacity together led to potent tumor therapeutic efficacy. The scalable and facile small molecule syntheses and potent antitumor efficacy make our drug amphiphiles promising for large-scale synthesis and clinical translation.

EXPERIMENTAL SECTION

Materials. Methyl isonipecotate, 1-ethyl-(3-dimethylaminopropyl)carbodiie hydrochloride (EDC·HCl), *N*-hydroxysuccinimide (NHS), *N,N*-diisopropylethylamine (DIPEA), and 4-(dimethylamino)pyridine (DMAP) were purchased from Sigma-Aldrich (St. Louis, MO). Camptothecin (CPT) was purchased from Fisher Scientific (Pittsburgh, PA). Radiometal [⁶⁴Cu] was produced by the PET Department, NIH Clinical Center. All other chemicals were purchased from Sigma-Aldrich (St. Louis, MO) and used without further purification unless otherwise noted. EB-NH₂ and EB-Lys-NOTA were synthesized as previously reported.^{25,26}

Instrumentation. The ¹H NMR spectra were collected on Bruker AV300 spectrometer at 300 MHz. Chemical shifts were referenced to

the solvent residual signals. UV-vis absorption spectra were recorded by using a GENESYS 10S UV-vis spectrophotometers (Thermal Fisher Scientific, Inc. Waltham, MA). All emission and excitation spectra and emission kinetics were obtained with a Horiba FluoroMax4 with automatic polarizers. Dynamic light scattering (DLS) measurements and the particle zeta potential values were determined using a The Horiba SZ-100 (HORIBA, Ltd., Kyoto, Japan) instrument equipped with a 10 mW laser diode operating at 532 nm. Transmission electron microscopy (TEM) was conducted on a FEI Tecnai electron microscope. The samples as aqueous solutions (4 μ L) were deposited onto carbon-coated copper grids, and after 1 min, the excess of the solution was quickly wicked away by a piece of filter paper. The grids were allowed to dry in air overnight. CPT-ss-EB/BSA nanocomplexes were stained by uranyl acetate.

Synthesis of 2. DMAP (1.05 g, 8.60 mmol) in 10 mL of dichloromethane (DCM) was dropwise added to a mixture suspension of CPT (1.0 g, 2.87 mmol) and triphosgene (0.315 g, 1.06 mmol) in anhydrous DCM (200 mL) under stirring. After stirring for 30 min, 2,2'-dithiodiethanol (8.60 g, 55.8 mmol) in anhydrous THF (25 mL) was added, and the reaction mixture was stirred overnight at room temperature. The mixture was washed with 50 mM HCl aqueous solution (2 \times 100 mL), water (1 \times 100 mL), and saturated brine (1 \times 100 mL). The organic layer was separated and dried over anhydrous Na₂SO₄. The solution was concentrated by rotary evaporator, and the residue was purified by flash chromatography (Teledyne ISCO CombiFlash) using a prepacked silica column. Gradient ethyl acetate and hexane mixture were used as eluent. Yield: 1.05 g (69% yield). ¹H NMR (300 MHz, CD₂Cl₂) δ 8.46 (s, 1H), 8.22 (d, *J* = 8.3 Hz, 1H), 7.99 (dd, *J* = 8.2, 1.1 Hz, 1H), 7.86 (ddd, *J* = 8.5, 6.9, 1.5 Hz, 1H), 7.70 (ddd, *J* = 8.1, 6.9, 1.2 Hz, 1H), 7.42 (s, 1H), 5.64 (d, *J* = 18 Hz, 1H), 5.36 (m, *J* = 18 Hz, 1H) 4.37 (t, *J* = 6.0 Hz, 2H), 3.93–3.81 (m, 2H), 3.03–2.82 (m, 4H), 2.19 (tdd, *J* = 14.0, 12.3, 7.5 Hz, 3H), 1.01 (t, *J* = 7.5 Hz, 3H).

Synthesis of 3. Succinic anhydride (400 mg, 4.00 mmol), **1** (204 mg, 0.386 mmol) and DMAP (19.6 mg, 0.161 mmol) were dissolved in anhydrous DCM (200 mL) under stirring. The reaction mixture was stirred overnight at room temperature and then was washed with water (1 \times 100 mL), 50 mM HCl aqueous solution (1 \times 100 mL), and saturated brine (1 \times 100 mL). The organic layer was separated and dried over anhydrous Na₂SO₄. The solution was concentrated by rotary evaporator, and the residue was purified by flash chromatography (Teledyne ISCO CombiFlash) using a prepacked silica column. Gradient ethyl acetate and hexane mixture were used as eluent. Yield: 201 mg (83% yield). ESI-MS *m/z*: calcd 628.12, found 629.10 (*M* + *H*). ¹H NMR (300 MHz, CDCl₃) δ 8.44 (s, 1H), 8.32 (d, *J* = 8.4 Hz, 1H), 7.95 (d, *J* = 8.2 Hz, 1H), 7.86 (ddd, *J* = 8.5, 6.9, 1.4 Hz, 1H), 7.69 (ddd, *J* = 8.1, 7.0, 1.1 Hz, 1H), 7.43 (s, 1H), 5.71 (d, *J* = 17.3 Hz, 1H), 5.39 (d, *J* = 17.3 Hz, 1H), 5.32 (s, 2H), 4.46–4.25 (m, 4H), 3.00–2.86 (m, 4H), 2.79–2.61 (m, 4H), 2.37–2.07 (m, 2H), 1.01 (t, *J* = 7.5, 3H).

Synthesis of 4. **3** (58 mg, 0.092 mmol), EB-NH₂ (25 mg, 0.046 mmol), benzotriazol-1-yl-oxytripyrrolidinophosphonium hexafluorophosphate (PyBOP, 48 mg, 0.092 mmol), and *N,N*-diisopropylethylamine (DIPEA, 59 mg, 0.46 mmol) were mixed in DMF and stirred for 2 days under nitrogen. The reaction was quenched by adding excess amount of acetic acid and purified by preparative HPLC using acetonitrile and 0.2% acetic acid in water (gradient: 5–95% of acetonitrile). The collected purified product was lyophilized and stored in –20 $^{\circ}$ C for later use. Yield: 21 mg (40% yield). ESI-MS *m/z*: calcd 1152.20, found 1151.20 (*M* – *H*). ¹H NMR (300 MHz, DMSO) δ 9.34 (s, 1H), 8.70 (d, *J* = 3.7 Hz, 1H), 8.35 (s, 1H), 8.21–8.10 (m, 3H), 8.02 (d, *J* = 9.9 Hz, 1H), 7.88 (dt, *J* = 8.4, 4.1 Hz, 2H), 7.73 (dd, *J* = 6.9, 4.1 Hz, 1H), 7.64 (d, *J* = 4.0 Hz, 2H), 7.56 (d, *J* = 6.5 Hz, 1H), 7.50 (d, *J* = 5.2 Hz, 2H), 7.09 (d, *J* = 2.2 Hz, 1H), 7.00 (d, *J* = 10.0 Hz, 1H), 5.52 (s, 2H), 5.32 (s, 3H), 4.32 (t, *J* = 5.9 Hz, 3H), 4.21 (t, *J* = 6.2 Hz, 2H), 3.55 (t, *J* = 6.4 Hz, 1H), 3.06–2.89 (m, 3H), 2.75 (dd, *J* = 11.9, 5.4 Hz, 1H), 2.66–2.52 (m, 6H), 2.28 (s, 3H), 2.26 (s, 3H), 2.22–2.13 (m, 4H), 0.91 (m, 3H).

Synthesis of 5. DMAP (1.68 g, 13.8 mmol) in 10 mL of DCM was dropwise added to a mixture suspension of CPT (1.5 g, 4.31 mmol)

and triphosgene (0.473 g, 1.59 mmol) in anhydrous DCM (200 mL) under stirring. After stirring for 30 min, 2,2'-dithiodiethanol (6.64 g, 43.1 mmol) in anhydrous THF (15 mL) was added, and the reaction mixture was stirred overnight at room temperature. The mixture was washed with 50 mM HCl aqueous solution (2 × 100 mL), water (1 × 100 mL), and saturated brine (1 × 100 mL). The organic layer was separated and dried over anhydrous Na₂SO₄. The solution was concentrated by rotary evaporator, and the residue was purified by flash chromatography (Teledyne ISCO CombiFlash) using a prepacked silica column. Gradient ethyl acetate and hexane mixture were used as eluent. Yield: 1.48 g (70% yield). ¹H NMR (300 MHz, CDCl₃) δ 8.41 (s, 1H), 8.23 (d, *J* = 8.7 Hz, 1H), 7.95 (dd, *J* = 8.2, 1.1 Hz, 1H), 7.85 (ddd, *J* = 8.5, 6.9, 1.5 Hz, 1H), 7.68 (ddd, *J* = 8.1, 6.9, 1.2 Hz, 1H), 7.36 (s, 1H), 5.70 (d, *J* = 17.3 Hz, 1H), 5.39 (d, *J* = 17.3 Hz, 1H), 5.30 (s, 2H), 4.21–4.05 (m, 2H), 3.59 (dd, *J* = 10.1, 6.1 Hz, 2H), 2.43–2.01 (m, 2H), 1.74–1.65 (m, 3H), 1.59–1.47 (m, 2H), 1.45–1.32 (m, 4H), 1.00 (t, *J* = 7.5 Hz, 3H).

Synthesis of 6. Succinic anhydride (400 mg, 4.00 mmol), **5** (200 mg, 0.406 mmol) and DMAP (19.8 mg, 0.162 mmol) were dissolved in anhydrous DCM (200 mL) under stirring. The reaction mixture was stirred overnight at room temperature and then washed with water (1 × 100 mL), 50 mM HCl aqueous solution (1 × 100 mL), and saturated brine (1 × 100 mL). The organic layer was separated and dried over anhydrous Na₂SO₄. The solution was concentrated by rotary evaporator, and the residue was purified by flash chromatography (Teledyne ISCO CombiFlash) using a prepacked silica column. Gradient ethyl acetate and hexane mixture were used as eluent. Yield: 192 mg (80% yield). ESI-MS *m/z*: calcd 592.21, found 591.25 (M – H). ¹H NMR (300 MHz, CDCl₃) δ 8.42 (s, 1H), 8.28 (d, *J* = 8.7 Hz, 1H), 7.95 (d, *J* = 8.3 Hz, 1H), 7.85 (ddd, *J* = 8.5, 6.9, 1.5 Hz, 1H), 7.68 (ddd, *J* = 8.1, 6.9, 1.1 Hz, 1H), 7.38 (d, *J* = 5.1 Hz, 1H), 5.70 (d, *J* = 17.3 Hz, 1H), 5.39 (d, *J* = 17.3 Hz, 1H), 5.31 (s, 2H), 4.23–3.99 (m, 4H), 2.74–2.56 (m, 4H), 2.37–2.07 (m, 3H), 1.61 (ddd, *J* = 19.2, 12.9, 6.6 Hz, 5H), 1.44–1.23 (m, 7H), 1.00 (t, *J* = 7.5 Hz, 3H).

Synthesis of 7. **6** (52 mg, 0.092 mmol), EB-NH₂ (25 mg, 0.046 mmol), PyBOP (48 mg, 0.092 mmol), and DIPEA (59 mg, 0.46 mmol) were mixed in DMF and stirred for 2 days under nitrogen. The reaction was quenched by adding an excess amount of acetic acid and purified by preparative HPLC using acetonitrile and 0.2% acetic acid in water (gradient: 5–95% of acetonitrile). The collected purified product was lyophilized and stored in –20 °C for later use. Yield: 23 mg (45% yield). ESI-MS *m/z*: calcd 1116.29, found 1115.36 (M – H). ¹H NMR (300 MHz, DMSO) δ 9.33 (s, 1H), 8.71 (d, *J* = 5.1 Hz, 1H), 8.35 (s, 1H), 8.22–8.10 (m, 3H), 8.05–8.00 (m, 1H), 7.92–7.83 (m, 3H), 7.77–7.53 (m, 6H), 7.51 (s, 1H), 7.05 (s, 1H), 6.99 (dd, *J* = 9.9, 3.4 Hz, 1H), 5.52 (s, 2H), 5.32 (d, *J* = 3.9 Hz, 2H), 4.09 (t, *J* = 6.4 Hz, 2H), 3.90 (t, *J* = 6.3 Hz, 2H), 3.66–3.56 (m, 2H), 3.28 (t, *J* = 6.2 Hz, 1H), 3.14 (dd, *J* = 7.4, 4.3 Hz, 1H), 2.76–2.54 (m, 6H), 2.28 (s, 3H), 2.26 (s, 3H), 2.16 (d, *J* = 7.8 Hz, 3H), 1.53 (d, *J* = 27.3 Hz, 4H), 1.35–1.18 (m, 19H), 0.91 (t, *J* = 7.3 Hz, 3H).

Synthesis of 8. **6** (27 μmol) and *N*-hydroxysuccinimide (27 μmol) were dissolved in 1.0 mL of dry THF at –10 °C. Then *N,N'*-dicyclohexylcarbodiimide (DCC, 27 μmol) in dry THF (0.5 mL) was added dropwise. The reaction mixture was stirred for 1 h at –10 °C and then overnight at room temperature. White precipitate was removed by filtration, and the solvent was removed *in vacuo* to obtain an oil. The product was recrystallized in ethyl acetate to obtain a white-yellow solid product (52% yield).

Synthesis of 9. EB-Lys-NOTA was synthesized according to the published procedure.²⁵ EB-Lys-NOTA (5.0 μmol) was dissolved in 200 μL of DMF. Then **8** (6.0 μmol) in 100 μL DMF was added, followed by addition of DIPEA (25 μmol). The reaction was stirred at room temperature for 3–4 h. Then, the crude was purified followed the published procedure using Higgins column.²⁵ The product was achieved with a chemical purity >95%. LCMS *m/z*: calcd 1530.52, found 1529.46 (M – H).

Synthesis of 11. To a solution of **6** (3.6 equiv) in 1.0 mL of anhydrous DMF were added (1-[bis(dimethylamino)methylene]-1H-1,2,3-triazolo[4,5-*b*]pyridinium 3-oxide hexafluorophosphate) (HATU, 4.2 equiv) as a solid under argon. The solution was stirred

for 10 min at room temperature. Then 10 equiv of DIPEA was added followed by addition of *N*-Boc ethylenediamine (1.0 equiv) in DMF. The reaction was stirred overnight at room temperature. DMF was removed using an oil vacuum pump, and the crude mixture was extracted using DCM/water. The organic layer was evaporated and then treated with TFA/DCM (1:1 v/v) for 1 h at room temperature. The mixture was purified on a C-18 preparative column to give CPT-NH₂ as a yellow solid (44% yield). ESI-MS *m/z*: calcd 634.26, found 635.87 (M + H).

Synthesis of 12. **11** (5.0 μmol) was dissolved in 200 μL of DMF. Then NOTA-NHS ester (6.0 μmol) in 100 μL of DMF was added, followed by addition of DIPEA (25 μmol). The reaction was stirred at room temperature for 3–4 h and then purified following the published procedure using a Higgins column. The product was achieved with a chemical purity >95%. LCMS *m/z*: calcd 919.40, found: 920.34 (M + H). Analytic HPLC and LC-MS were used to confirm the purity.

CPT Release from Nanoparticles. The release of CPT from CPT-cc-EB and CPT-ss-EB was measured by a dialysis method. Briefly, CPT-cc-EB, CPT-ss-EB, or CPT-ss-EB/BSA complexes in water were diluted with phosphate buffered saline (PBS), yielding a concentration of 55 μg/mL, and 0.5 mL was transferred into presoaked dialysis cassettes (MWCO: 10 kDa) and dialyzed against 25 mL PBS or PBS with different concentrations of glutathione (GSH) at 37 °C for 72 h, respectively. Aliquots (0.1 mL) were taken at predetermined times from dialysate, and 0.1 mL of fresh PBS was added back into outside dialysate. Alternatively, 2.0 mL of CPT-ss-EB/BSA complexes (CPT-ss-EB concentration: 0.2 mg/mL, BSA concentration: 35 mg/mL) were incubated in a 20 mL vial at 37 °C for 72 h. Aliquots (0.1 mL) were taken at predetermined times from the solution. The increase of CPT concentration was monitored by HPLC (condition: 30% acetonitrile with 0.1% TFA, 1 mL/min, UV detector at 250 nm). The release was evaluated in triplicate.

Critical Aggregation Concentration (CAC) Measurement. Pyrene was used as a fluorescence probe to study the CAC of CPT-ss-EB according literature.^{7,36} Briefly, CPT-ss-EB was dispersed in water at 1.0 mg/mL with an aqueous solution of pyrene of 6.0 × 10^{–7} mol/L. Then the solution was diluted to various concentrations from 284 μg/mL to 0.277 μg/mL with a constant pyrene concentration of 6.0 × 10^{–7} mol/L. The excitation spectra of all samples were recorded, with the emission wavelength set at 375 nm. The *I*₃₃₀/*I*₃₃₅ ratio values of all solutions were determined, and the values were used to plot against concentration on a log scale. The CAC values were determined to be 1.5 μg/mL in water.

Kinetic Binding Assay of CPT-ss-EB with BSA by Biolayer Interferometry (BLI). The BLI measurement was performed on an Octet Red96 system using streptavidin biosensors (fortéBio) to determine the binding affinity of CPT-ss-EB, CPT-cc-EB, NOTA-CPT-EB, and CPT with biotinylated BSA. Assays were conducted in solid black 96-well plates under shaking (Geiger Bio-One) using a 7-step protocol: 1, baseline (1 × PBS), time: 60 s; 2, loading (biotinylated albumin, 1 μg/mL), time: 600 s; 3, baseline (1 × PBS), time: 60 s; 4, quenching (1 μg/mL biocytin (Thermo Scientific)), time: 180 s; 5, baseline (1 × PBS), time: 60 s; 6, association, time: 600 s; 7, dissociation, time: 600 s. Nonspecific binding was determined by measuring binding of albumin-loaded biosensor to buffer alone and blank biosensor to analytes. The obtained data were fitted using Octet Analysis software 7.0, and the fitted curve was used to calculate the dissociation constant using GraphPad Prism 7 (La Jolla, CA).

Molecular Docking of CPT-ss-EB into the Human Serum Albumin (HSA). The AutoDock program package version 4.2.6 (7) was used to perform automated molecular docking. The detailed process on model construction, molecular docking, and binding affinity prediction is described in [Supporting Information](#).

In Vitro Cytotoxicity Assays. Human glioma cell line U87MG, human colon cancer cells HCT116, human lung carcinoma cell line A549, or the mouse mammary carcinoma 4T1 were plated in 96-well plates in minimum essential media (MEM) (U87MG), McCoy's 5a medium (HCT116), F-12K medium (A549), or RPMI-1640 medium (4T1) (10% fetal bovine serum and 1% penicillin). Cells were

incubated at 37 °C in a humidified atmosphere containing 5% CO₂. The medium was replaced with fresh medium 24 h after seeding. Formulations of CPT derivatives were dissolved in PBS and diluted using cell culture medium. For each well, 100 μL of cell culture medium with different designated drug concentrations was added. Negative controls were created by addition of 100 μL of culture medium. The cells were incubated for 48 h, and after this period, the medium was replaced with 100 μL medium containing 0.5 mg/mL of 3-(4,5-dimethylthiazol-2-yl)-2,5-diphenyltetrazolium (MTT). After the cells were incubated with the reagent for 2 h, the medium containing unreacted MTT was carefully removed. Then, the obtained blue formazan crystals were dissolved in 100 μL of DMSO, and the absorbance was measured in a BioTek Synergy H4 hybrid reader at a wavelength of 570 nm. The blank was subtracted to the measured optical density (OD) values, and the cell viability was calculated based on the relative absorbance to the control untreated cells. The calculation of the IC₅₀ values and the statistical analysis were performed using GraphPad Prism 5.

In Vitro Cell Uptake. *In vitro* cell uptake was studied using confocal laser scanning microscopy and flow cytometry. CPT-ss-EB (10 μM) was incubated with HCT116 cells for 2 or 4 h (1 h for super resolution single cell confocal microscopy) and stained with Lysotracker Green (Life Technologies, Carlsbad, CA) and 10 μg/mL of Hoechst 33342 (Life Technologies, Carlsbad, CA), or stained with SYTO 9 (Life Technologies, Carlsbad, CA), for 0.5 h in a cell culture incubator at 37 °C before confocal observation. Cells were then washed with Dulbecco's PBS for three times before imaging. Conventional confocal microscopy was conducted on a Zeiss LSM 780 confocal microscope (Chesterfield, VA). Super resolution confocal microscopy was conducted on a Leica SP5 confocal microscope. Alternatively, for flow cytometric analysis, HCT116 cells were seeded into a 24-well plate, and 24 h later, cells were treated with CPT-ss-EB, CPT-cc-EB, CPT, irinotecan (IR), and EB-amine (10 μM for each drug) for 4 h. Then, cells were detached using trypsin and washed with Dulbecco's PBS for three times. The fluorescence intensities of cells were analyzed using a BD Beckman Coulter flow cytometer (Brea, CA). EB fluorescence: excitation, 532 nm; emission, 660 nm, and CPT fluorescence: excitation, 355 nm, emission, 450 nm.

In Vivo PET Imaging of HCT116 Tumor. All animal work was conducted in accordance to the NIH Guide for the Care and Use of Animals under protocols approved by the NIH Clinical Center Animal Care and Use Committee. HCT116 tumor-bearing nude mice (7 weeks old, female) were prepared by subcutaneously injection of a suspension of 5 × 10⁶ HCT116 cells in PBS (100 μL). When the tumor sizes reached 500–1000 mm³, mice were used for PET imaging. Mice were anesthetized using isoflurane/O₂ (2% v/v) before tracer injection. Anesthetized mice were injected intravenously with ⁶⁴Cu-labeled drug (4.44–5.55 MBq/120–150 μCi per mouse) in PBS (100 μL). At indicated time points post-injection, mice were scanned on an Inveon DPET scanner (Siemens Medical Solutions, Malvern, PA). PET images were reconstructed without correction for attenuation or scattering using a 3D ordered subset expectation maximization algorithm. ASI Pro VM software was used for image analysis. Regions of interest (ROI) were drawn on any organs of interest to calculate the %ID/g.

The above mice were sacrificed at 48 h post-injection. Organs and blood were collected and wet-weighted. The collected organs and blood, together with a series of standard solution, were measured for ⁶⁴Cu radioactivity on a γ-counter (Wallac Wizard 1480, PerkinElmer). The radioactivity of organs and blood was converted to calculate the percentages of the injected dose (%ID) in organs of interest and the percentages of the injected dose per gram of tissue (%ID/g).

In Vivo Therapy with HCT116 Tumor-Bearing Mice. All animal work was conducted in accordance to the NIH Guide for the Care and Use of Animals under protocols approved by the NIH Clinical Center Animal Care and Use Committee. HCT116 tumor-bearing nude mice (7 weeks old, female) were prepared by subcutaneously injection of a suspension of 5 × 10⁶ HCT116 cells in PBS (100 μL). When the tumor was established on day 10 post-tumor inoculation, mice started to be treated with specified regimens by intravenous injection of 100

μL of drugs or PBS every 3 days for a maximum of 5 times (dose of CPT/IR equivalents: 3 mg/kg). Tumor volume and mouse weight were monitored every 3 days. Mice were euthanized when any dimension of tumor exceeded 2 cm or when mouse weight lost by over 20%. The volume for each type of tumor was respectively calculated using the following formula:

$$\text{volume} = (\text{length} \times \text{width}^2)/2$$

Results were analyzed using GraphPad Prism 7 (La Jolla, CA).

ASSOCIATED CONTENT

Supporting Information

The Supporting Information is available free of charge on the ACS Publications website at DOI: 10.1021/acsnano.7b03003.

The synthetic schemes and characterizations of CPT-cc-EB, NOTA-EB-CPT, and NOTA-CPT as well as additional *in vitro* and *in vivo* characterization of prodrug amphiphiles (PDF)

Video S1: Sharp contrast between the accumulation of CPT-EB and CPT in tumor (MPG)

AUTHOR INFORMATION

Corresponding Authors

*E-mail: guizhi.zhu@nih.gov.

*E-mail: shawn.chen@nih.gov.

ORCID

Zhen Yang: 0000-0003-4056-0347

Xiaoyuan Chen: 0000-0002-9622-0870

Notes

The authors declare no competing financial interest.

ACKNOWLEDGMENTS

This work is supported by the Intramural Research Program of NIBIB, NIH. Y.L. was also supported by the National Science Foundation of China (81601531) and National Science Foundation of Jiangsu Province (BK20160755). We thank Mr. Geoffrey Daniels at Leica Microsystems Inc. for technical assistance with super resolution imaging and image analysis, and Drs. Jennie Garcia-Olivares and Francisco J. Palma-Cerda at NIH for help with BLI studies.

REFERENCES

- (1) Siegel, R. L.; Miller, K. D.; Jemal, A. *Cancer Statistics, 2017*. *Ca-Cancer J. Clin.* **2017**, *67*, 7–30.
- (2) Siegel, R.; DeSantis, C.; Jemal, A. *Colorectal Cancer Statistics, 2014*. *Ca-Cancer J. Clin.* **2014**, *64*, 104–117.
- (3) Pommier, Y. Topoisomerase I Inhibitors: Camptothecins and Beyond. *Nat. Rev. Cancer* **2006**, *6*, 789–802.
- (4) Su, H.; Zhang, P. C.; Cheetham, A. G.; Koo, J. M.; Lin, R.; Masood, A.; Schiapparelli, P.; Quinones-Hinojosa, A.; Cui, H. G. Supramolecular Crafting of Self-Assembling Camptothecin Prodrugs with Enhanced Efficacy against Primary Cancer Cells. *Theranostics* **2016**, *6*, 1065–1074.
- (5) Cai, K. M.; He, X.; Song, Z. Y.; Yin, Q.; Zhang, Y. F.; Uckun, F. M.; Jiang, C.; Cheng, J. J. Dimeric Drug Polymeric Nanoparticles with Exceptionally High Drug Loading and Quantitative Loading Efficiency. *J. Am. Chem. Soc.* **2015**, *137*, 3458–3461.
- (6) Xu, Y.; Villalona-Calero, M. A. Irinotecan: Mechanisms of Tumor Resistance and Novel Strategies for Modulating its Activity. *Ann. Oncol.* **2002**, *13*, 1841–1851.
- (7) Liu, J. Y.; Liu, W. E.; Weitzhandler, I.; Bhattacharyya, J.; Li, X. H.; Wang, J.; Qi, Y. Z.; Bhattacharjee, S.; Chilkoti, A. Ring-Opening Polymerization of Prodrugs: A Versatile Approach to Prepare Well-

Defined Drug-Loaded Nanoparticles. *Angew. Chem., Int. Ed.* **2015**, *54*, 1002–1006.

(8) Cheetham, A. G.; Zhang, P. C.; Lin, Y. A.; Lock, L. L.; Cui, H. G. Supramolecular Nanostructures Formed by Anticancer Drug Assembly. *J. Am. Chem. Soc.* **2013**, *135*, 2907–2910.

(9) Huang, P.; Wang, D. L.; Su, Y.; Huang, W.; Zhou, Y. F.; Cui, D. X.; Zhu, X. Y.; Yan, D. Y. Combination of Small Molecule Prodrug and Nanodrug Delivery: Amphiphilic Drug-Drug Conjugate for Cancer Therapy. *J. Am. Chem. Soc.* **2014**, *136*, 11748–11756.

(10) Liao, L. Y.; Liu, J.; Dreaden, E. C.; Morton, S. W.; Shopsowitz, K. E.; Hammond, P. T.; Johnson, J. A. A Convergent Synthetic Platform for Single-Nanoparticle Combination Cancer Therapy: Radiometric Loading and Controlled Release of Cisplatin, Doxorubicin, and Camptothecin. *J. Am. Chem. Soc.* **2014**, *136*, 5896–5899.

(11) Lee, M. H.; Sessler, J. L.; Kim, J. S. Disulfide-Based Multifunctional Conjugates for Targeted Theranostic Drug Delivery. *Acc. Chem. Res.* **2015**, *48*, 2935–2946.

(12) Bhuniya, S.; Maiti, S.; Kim, E. J.; Lee, H.; Sessler, J. L.; Hong, K. S.; Kim, J. S. An Activatable Theranostic for Targeted Cancer Therapy and Imaging. *Angew. Chem., Int. Ed.* **2014**, *53*, 4469–4474.

(13) Elsbahy, M.; Heo, G. S.; Lim, S. M.; Sun, G. R.; Wooley, K. L. Polymeric Nanostructures for Imaging and Therapy. *Chem. Rev.* **2015**, *115*, 10967–11011.

(14) Min, Y. Z.; Caster, J. M.; Eblan, M. J.; Wang, A. Z. Clinical Translation of Nanomedicine. *Chem. Rev.* **2015**, *115*, 11147–11190.

(15) Zhang, F. W.; Zhang, S. Y.; Pollack, S. F.; Li, R. C.; Gonzalez, A. M.; Fan, J. W.; Zou, J.; Leininger, S. E.; Pavia-Sanders, A.; Johnson, R.; Nelson, L. D.; Raymond, J. E.; Elsbahy, M.; Hughes, D. M. P.; Lenox, M. W.; Gustafson, T. P.; Wooley, K. L. Improving Paclitaxel Delivery: *In Vitro* and *In Vivo* Characterization of PEGylated Polyphosphoester-Based Nanocarriers. *J. Am. Chem. Soc.* **2015**, *137*, 2056–2066.

(16) Yu, G. C.; Zhao, R.; Wu, D.; Zhang, F. W.; Shao, L.; Zhou, J.; Yang, J.; Tang, G. P.; Chen, X. Y.; Huang, F. H. Pillar[5]arene-Based Amphiphilic Supramolecular Brush Copolymers: Fabrication, Controllable Self-assembly and Application in Self-imaging Targeted Drug Delivery. *Polym. Chem.* **2016**, *7*, 6178–6188.

(17) Tan, X. Y.; Li, B. B.; Lu, X. G.; Jia, F.; Santori, C.; Menon, P.; Li, H.; Zhang, B. H.; Zhao, J. J.; Zhang, K. Light-Triggered, Self-Immolative Nucleic Acid-Drug Nanostructures. *J. Am. Chem. Soc.* **2015**, *137*, 6112–6115.

(18) Lee, M. H.; Kim, E. J.; Lee, H.; Kim, H. M.; Chang, M. J.; Park, S. Y.; Hong, K. S.; Kim, J. S.; Sessler, J. L. Liposomal Texaphyrin Theranostics for Metastatic Liver Cancer. *J. Am. Chem. Soc.* **2016**, *138*, 16380–16387.

(19) Hu, M. X.; Huang, P.; Wang, Y.; Su, Y.; Zhou, L. Z.; Zhu, X. Y.; Yan, D. Y. Synergistic Combination Chemotherapy of Camptothecin and Floxuridine through Self-Assembly of Amphiphilic Drug-Drug Conjugate. *Bioconjugate Chem.* **2015**, *26*, 2497–2506.

(20) Ma, Y.; Mou, Q.; Zhu, X.; Yan, D. Small Molecule Nanodrugs for Cancer Therapy. *Mater. Today Chem.* **2017**, *4*, 26–39.

(21) Mou, Q.; Ma, Y. B.; Zhu, X. Y.; Yan, D. Y. A Small Molecule Nanodrug Consisting of Amphiphilic Targeting Ligand-Chemotherapy Drug Conjugate for Targeted Cancer Therapy. *J. Controlled Release* **2016**, *230*, 34–44.

(22) Shen, Y. Q.; Jin, E. L.; Zhang, B.; Murphy, C. J.; Sui, M. H.; Zhao, J.; Wang, J. Q.; Tang, J. B.; Fan, M. H.; Van Kirk, E.; Murdoch, W. J. Prodrugs Forming High Drug Loading Multifunctional Nanocapsules for Intracellular Cancer Drug Delivery. *J. Am. Chem. Soc.* **2010**, *132*, 4259–4265.

(23) Maeda, H.; Wu, J.; Sawa, T.; Matsumura, Y.; Hori, K. Tumor Vascular Permeability and the EPR Effect in Macromolecular Therapeutics: a Review. *J. Controlled Release* **2000**, *65*, 271–284.

(24) Owen, S. C.; Chan, D. P. Y.; Shoichet, M. S. Polymeric Micelle Stability. *Nano Today* **2012**, *7*, 53–65.

(25) Chen, H.; Jacobson, O.; Niu, G.; Weiss, I. D.; Kiesewetter, D. O.; Liu, Y.; Ma, Y.; Wu, H.; Chen, X. Novel Molecular “Add-on” Based on Evans Blue Confers Superior Pharmacokinetics and Transforms Drugs to Theranostic Agents. *J. Nucl. Med.* **2017**, *58*, 590–597.

(26) Niu, G.; Lang, L. X.; Kiesewetter, D. O.; Ma, Y.; Sun, Z. C.; Guo, N.; Guo, J. X.; Wu, C. X.; Chen, X. Y. *In Vivo* Labeling of Serum Albumin for PET. *J. Nucl. Med.* **2014**, *55*, 1150–1156.

(27) Jacobson, O.; Kiesewetter, D. O.; Chen, X. Albumin-Binding Evans Blue Derivatives for Diagnostic Imaging and Production of Long-Acting Therapeutics. *Bioconjugate Chem.* **2016**, *27*, 2239–2247.

(28) Liu, Y.; Wang, G.; Zhang, H.; Ma, Y.; Lang, L.; Jacobson, O.; Kiesewetter, D. O.; Zhu, L.; Gao, S.; Ma, Q.; Chen, X. Stable Evans Blue Derived Exendin-4 Peptide for Type 2 Diabetes Treatment. *Bioconjugate Chem.* **2016**, *27*, 54–58.

(29) Merlot, A. M.; Kalinowski, D. S.; Richardson, D. R. Unraveling the Mysteries of Serum Albumin—More Than Just a Serum Protein. *Front. Physiol.* **2014**, *5*, 299.

(30) Matsumura, Y.; Maeda, H. A New Concept for Macromolecular Therapeutics in Cancer-Chemotherapy - Mechanism of Tumoritropic Accumulation of Proteins and the Antitumor Agent Smancs. *Cancer Res.* **1986**, *46*, 6387–6392.

(31) Liu, H. P.; Moynihan, K. D.; Zheng, Y. R.; Szeto, G. L.; Li, A. V.; Huang, B.; Van Egeren, D. S.; Park, C.; Irvine, D. J. Structure-Based Programming of Lymph-Node Targeting in Molecular Vaccines. *Nature* **2014**, *507*, 519–522.

(32) Kratz, F. Albumin as a Drug Carrier: Design of Prodrugs, Drug Conjugates and Nanoparticles. *J. Controlled Release* **2008**, *132*, 171–183.

(33) Miele, E.; Spinelli, G. P.; Miele, E.; Tomao, F.; Tomao, S. Albumin-Bound Formulation of Paclitaxel (Abraxane (R) ABI-007) in the Treatment of Breast Cancer. *Int. J. Nanomed.* **2009**, *4*, 99–105.

(34) Burke, T. G.; Mi, Z. H. The Structural Basis of Camptothecin Interactions with Human Serum-Albumin - Impact on Drug Stability. *J. Med. Chem.* **1994**, *37*, 40–46.

(35) Wilhelm, S.; Tavares, A. J.; Dai, Q.; Ohta, S.; Audet, J.; Dvorak, H. F.; Chan, W. C. W. Analysis of Nanoparticle Delivery to Tumours. *Nat. Rev. Mater.* **2016**, *1*, 16014.

(36) Wilhelm, M.; Zhao, C. L.; Wang, Y. C.; Xu, R. L.; Winnik, M. A.; Mura, J. L.; Riess, G.; Croucher, M. D. Poly(Styrene-Ethylene Oxide) Block Copolymer Micelle Formation in Water - a Fluorescence Probe Study. *Macromolecules* **1991**, *24*, 1033–1040.